Carbon 228 (2024) 119356

Contents lists available at ScienceDirect

Carbon

journal homepage: www.elsevier.com/locate/carbon

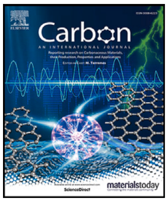

Research paper

Improved understanding of carbon nanotube growth via autonomous jump regression targeting of catalyst activity

Robert Waelder [a,b], Chiwoo Park [c], Arthur Sloan [a,d], Jennifer Carpena-Núñez [a,b], Joshua Yoho [a,b], Stephane Gorsse [e], Rahul Rao [a], Benji Maruyama [a,*]

[a] Materials and Manufacturing Directorate, Air Force Research Laboratory, Wright-Patterson Air Force Base, 45433, OH, USA
[b] UES, Inc., 4401 Dayton-Xenia Rd, Dayton, 45432, OH, USA
[c] Department of Industrial Systems Engineering, University of Washington, Box 352650, Seattle, 98195, WA, USA
[d] National Research Council, 500 5th St NW, Washington, 20001, DC, USA
[e] CNRS, University Bordeaux, ICMCB, UPR 9048, Bordeaux INP, 33600, Pessac, France

ARTICLE INFO

Keywords:
Carbon nanotube synthesis
Autonomous experimentation
ARES
Ostwald ripening
Oxidation/reduction
Supported catalyst chemical vapor deposition

ABSTRACT

Catalyst control is critical to carbon nanotube (CNT) growth and scaling their production. In supported catalyst CNT growth, the reduction of an oxidized metal catalyst enables growth, but its reduction also initiates catalyst deactivation via Ostwald ripening. Here, we conducted autonomous experiments guided by a hypothesis-driven machine learning planner based on a novel jump regression algorithm. This planning algorithm iteratively models the experimental response surface to identify discontinuities, such as those created by a material phase change, and targets further experiments to improve the fit and reduce uncertainty in its model. This approach led us to identify conditions that resulted in the greatest CNT yields as a function of the driving forces of catalyst reduction in a fraction of the time and cost of conventional experimental approaches. By varying temperature and the reducing potential of the growth atmosphere, we identified discontinuous jumps in CNT growth for two thicknesses of an iron catalyst, resulting in largest observed yields in narrow and distinct regions of thermodynamic space where we believe the reduced catalyst is in equilibrium with its oxide. At these jumps, we also observed the longest growth lifetimes and a greater degree of diameter control. We believe that conducting CNT growth at these conditions optimizes catalyst activity by inhibiting Ostwald ripening-induced deactivation, thereby keeping catalyst nanoparticles smaller and more numerous. This work establishes a thermodynamic framework for a generalized understanding of metal catalysts in CNT growth, and demonstrates the capability of iterative, hypothesis-driven autonomous experimentation to greatly accelerate materials science.

1. Introduction

Carbon nanotubes (CNTs) are a promising material with myriad applications, including conventional [1–3] and flexible [4] electronics, and their strength to weight ratio makes them an ideal component in structural composite materials [5–7]. Despite more than two decades of development as a high performance material [8], CNT synthesis remains a poorly understood process, due in part to the slow pace of research: typically 1–2 experiments per day. Understanding of CNT growth has increased tremendously due to experimental [9–13] and computational [14–19] efforts, but faster, hypothesis-driven, iterative search is required for further understanding, ultimately leading to commercialization [20].

A major component in understanding CNT growth, particularly single-walled CNT growth, is understanding catalyst behavior. Catalyst morphology has been shown to have a strong effect on several CNT growth parameters [21], particularly as it relates to CNT diameters [22–24]. Diameter and helicity control of CNTs is critical for conductivity in aligned CNT materials [25], properties such as plasmon resonances [26], as well as applications such as molecular transport [27] and field emission [28].

In supported catalyst chemical vapor deposition, the catalyst is typically a thin film of a transition metal deposited on a substrate, often using an additional support layer between the substrate and catalyst [29]. A critical step in the CNT growth process is reducing the oxidized catalyst, activating it. This is often performed as its own step, by exposing the thin film catalyst oxide to high temperatures and

---

* Corresponding author.
E-mail address: benji.maruyama@us.af.mil (B. Maruyama).

https://doi.org/10.1016/j.carbon.2024.119356
Received 19 December 2023; Received in revised form 31 May 2024; Accepted 14 June 2024

reducing atmospheres (e.g., H_2). The reduced catalyst film dewets the surface and forms metallic nanoparticles capable of seeding the growth of CNTs once carbon sources are introduced. Once reduced, the active catalyst particles continue to evolve through Ostwald ripening [30], evaporation, migration [31], and other processes [32–35], ultimately terminating CNT growth. The rates of these mechanisms are dependent on the growth environment. These environmental effects can broadly be categorized as oxidizing or reducing conditions relative to the catalyst material, and are a function of temperature and growth atmosphere composition. Ostwald ripening in particular is slowed by the addition of water: oxidation and hydroxyl species reduce catalyst diffusion rates, prolonging the life of active catalysts [30].

Performing CNT growth experiments in a high-throughput, autonomous experiment system enables searching over a broad range of growth conditions across multiple reactor parameters. Using this system, we have previously shown that CNT yield can be maximized for a fixed set of reactor conditions by choice of iron/carbon catalyst composition [36]. By controlling temperature and gas flow rates to modulate oxidizing and reducing conditions for fixed iron catalyst thicknesses, here we show we can optimize CNT growth by tailoring the reaction parameters to a specific catalyst, and believe it can be generalized to arbitrary catalysts. We propose that these optimal reactor conditions originate from controlled Ostwald ripening; CNT growth in an environment that is as oxidizing as possible slows the Ostwald ripening rate, prolonging the early stages of catalyst development, when the dewetted metallic nanoparticles are smallest and most numerous. This results in increased catalyst activity and lifetime, increasing CNT yields, prolonging growth, and producing smaller and more consistent CNT diameters due to the size distribution of the nanoparticles [30].

2. Methods

Experiments are carried out using a cold-walled supported catalyst chemical vapor deposition system built on the ARES (Automated Research System) platform [37,38]. This system is able to perform CNT growth experiments on the order of minutes, while using *in-situ* Raman spectroscopy to characterize and apply the results through planning algorithms to determine the next experiment to run [39].

The supported catalyst structure is built up in three layers: from top to bottom, these are the thin film Fe catalyst, an Al_2O_3 support layer, and the Si/SiO_2 substrate. A grid of $10\,\mu m$ diameter pillars are etched into the substrate, thermally isolating each pillar. A $532\,nm$ Nd:YAG laser is used to heat each pillar individually, and the scattered laser light is directed into a Raman spectrometer, enabling *in situ* Raman spectra to be collected for yield and growth rate information, as well as temperature control. Further details on the experimental setup, including schematics, can be found in previous works [21,36–38,40,41]. The temperature-dependent Si Stokes Raman peak at $520.5\,cm^{-1}$ provides feedback to modulate laser power and maintain the desired temperature. A constant $10\,Torr$ growth atmosphere is created by mixing C_2H_4 and pre-mixed CO_2/Ar gasses of 0.1%, 1%, and 10% CO_2. Since C_2H_4 is highly reducing to the catalyst, CO_2 is employed to control the oxidation/reduction potential of the growth atmosphere. Latent water in the growth chamber is measured by a hygrometer and ranged from 0.8 to 2.5 ppm throughout all experiments conducted. The entire growth is performed as a single step; no separate catalyst reduction or heat treating steps are performed.

Two experimental campaigns were conducted using different catalyst thicknesses. In both cases, $10\,nm$ of Al_2O_3 is deposited by atomic layer deposition on top of the silicon pillars to serve as catalyst support. The Fe catalyst is then deposited by sputtering at thicknesses of $1\,nm$ and $0.3\,nm$ and allowed to oxidize upon removal from the deposition chamber. Experiments within each campaign are planned according to temperature and the log ratio of the partial pressures of ethylene and carbon dioxide.

For each experiment, the *in situ* and post-growth Raman spectra are used to confirm the growth temperature and determine CNT yield, growth rates, and nanotube diameters, where RBMs are present. CNT growth rates are determined by the change in area under the G band of the *in situ* Raman spectra, normalized by the area of the Si Raman peak at $520.5\,cm^{-1}$. The post-growth spectra are normalized by the area under the silicon peak to ensure comparability between experiments, and the CNT yield is calculated by integrating the G band between $1525\,cm^{-1}$ and $1650\,cm^{-1}$ after subtracting the noise floor, which we have previously used as a proxy yield metric [21,36,38,40,42]. Figure S1 shows sample Raman spectra and scanning electron microscope images for high, medium, and low yield results, where the abundance of CNTs in each image correlates to the relative yield from the Raman spectra. The weighted average of the radial breathing mode (RBM) region of the CNT Raman spectrum is used to determine the average diameter of the CNTs [11] in each growth experiment where RBM peaks are observed.

3. Results and discussion

The campaigns are conducted in two phases: an exploration phase to collect seed data, and an autonomous phase, where experiments are selected by a jump regression active learning planner [43,44]. Active learning is a machine learning technique where the model being trained is able to ask for new data. Although an established small data technique in the machine learning and artificial intelligence communities, it is a newcomer to materials science and physical experimentation more broadly. As such, the terminology is not yet fully cemented, and several terms are often used interchangeably. The term “planner” is often used to encompass the function of the computer and machine learning portion of the experiment, and contains two major parts: the model and the decision policy. The model is simply the mathematical representation of the output(s) as a function of the input(s). Output(s) are determined by an objective function, whose role is to determine a scalar value or small set of scalar values that extract the desired quality (e.g. yield, defect density, concentration, etc.), from a characterization technique, such as spectroscopy or imaging. In the case of one output measured as a function of two inputs, the model can be conceptualized as a surface in 3D space, and although the model can have arbitrary dimensionality, it is from this 3D conceptualization that it gets its other name: a response surface, where experimental outputs area represented by a surface that is a function of the experimental inputs. Equally important to the planner is the decision policy, also called an acquisition function. The decision policy is the component of the planner that actually designs experimental inputs by analyzing the model and deciding what experiment(s) should be done next based on according to the objectives and constraints of the experimental campaign as described by the researchers [39].

In the context of an autonomous research experimental campaign, this training loop is summarized as plan, experiment, analyze [39]. In the plan stage, the algorithm builds a surrogate mathematical model of the experimental response surface, and chooses an experiment which it believes will further the design goal of the campaign (e.g. minimize or maximize a response). The experiment stage then conducts the experiment with the requested conditions, and collects data to quantify the results. From there, the analyze stage quantifies the results according to the objective function, which handed back to the plan stage to update the model and repeat the process. The behavior of these planning algorithms are often explained in terms of exploration vs. exploitation search strategies. Exploration is experimenting in sparsely sampled regions of experimental space with high uncertainty to find features of interest. Exploitation is experimenting within a feature of interest to better understand features of interest and identify optimal conditions within the feature. These two phases of planning can be done simultaneously, alternating between sampling methods, or sequentially,

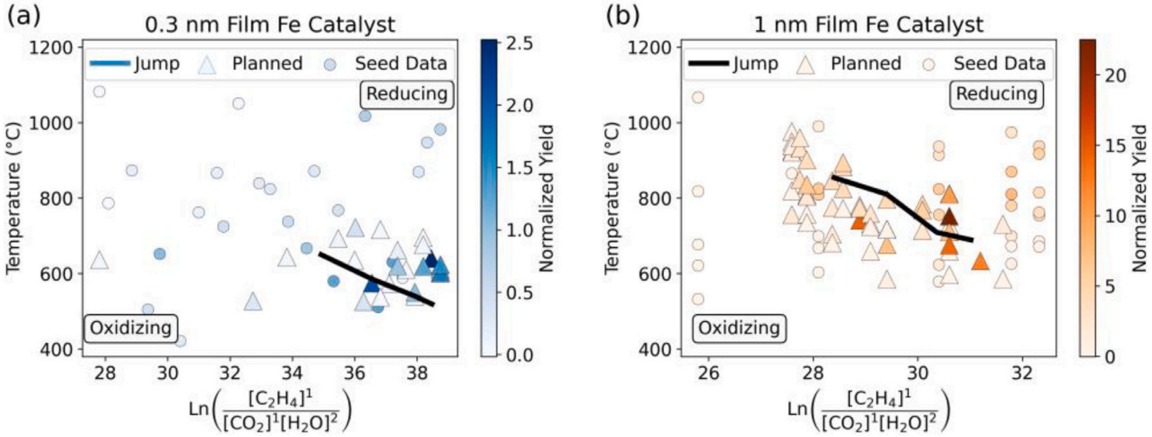

Fig. 1. CNT yield as a function of temperature and reducing potential of the growth gases, expressed as the log ratio of the partial pressures of ethylene, carbon dioxide, and latent water. The planned experiments targeting the jump in yield (triangles, circles are seed experiments) were designed by the jump regression planner (final jump boundary shown as black splines), and establish peak CNT growth conditions, with poorer yield both above and below the jump. In the 0.3 nm (a) campaign, the planned experiments achieved a maximum yield two times greater than maximum seed experiment yield, and similarly, the 1 nm (b) campaign planned experiments maximum yield is three times greater than the maximum seed data yield.

where the entire space is explored first with low resolution, followed by exploitation of the various features.

For the campaigns conducted in this work, we opted for the serial approach of distinct exploration and exploitation phases. For the exploration phase, seed points were determined by a simple space-filling design for the 1 nm catalyst film and by a Latin hypercube design for the 0.3 nm film. Latin hypercube sampling divides a space into a square grid, and selects experiments to sample each row and column only once [45]. This sampling provides a low resolution map of the whole experiment space, an ideal starting point for the optimization problem handled by the second phase of the campaign.

Jump regression is a new technique used to identify discontinuities in data and fit piecewise Gaussian process response surfaces using independent regression models separated by these discontinuities [43]. The planner begins with a single, continuous response surface, and when a threshold is met in the slope of the surface, the surface is split into multiple piecewise-defined surfaces separated by jump discontinuities. Future experiments are then selected based on a mean square prediction error criteria to improve the estimation of the jump locations based on past results [44]. While ordinary Gaussian processes are known to handle discontinuous response surfaces gracefully, the jump regression technique is distinct in that it is designed to target the jump(s). The result is a collection of connected points on one or more splines that represent the jump discontinuity.

We expect a discontinuity in the response surface due to a few possible factors: iron oxide does not catalyze CNT growth and must undergo a phase change to facilitate the reaction, and in addition, CNT synthesis has been demonstrated to require an activation energy to diffuse carbon atoms through the active catalyst material [46–48] below which CNTs will not grow. By incorporating these expected dynamics into the experiment planning algorithm, we create a physics-aware model more capable of identifying the area of interest in the response surface. The first 25 experiments for the 0.3 nm campaign are performed according to a Latin hypercube design, followed by additional iterations of five experiments targeted by the jump regression planner for a total of 50 experiments. A similar procedure is followed for the 1 nm campaign, with 32 seed experiments chosen by a space-filling design, followed by 53 jump regression-planned experiments. This directed, iterative, and hypothesis-informed approach to experimental design significantly reduces the required time and without sacrificing fidelity compared to conventional full-factorial experimental campaign approaches.

Fig. 1 shows the yield results of each catalyst campaign. Circles represent experiments part of the seed data and triangles are used for the jump regression planned experiments. Darker filled color indicates a greater CNT yield. The final jump spline identified in each experimental campaign is overlaid to each set of results in black. Growth in the 1 nm campaign tapered off at the most reducing end of the campaign, so further reducing conditions were not explored. Greater yields were observed for the 1 nm catalyst compared to the 0.3 nm catalyst, due to the increased catalyst volume and the longer lifetimes shown in Fig. 3. Additionally, the thinner catalyst film will be more affected by catalyst mass loss due to subsurface diffusion [33]. Identifying and targeting the jump enabled the planner to achieve double and triple the greatest CNT yields compared to the 0.3 nm and 1 nm campaign seed experiments, respectively.

Towards our hypothesis, in both campaigns, the best growth occurs along, or otherwise very near, the jump spline, with little growth occurring under less reducing conditions (lower temperature, lower C_2H_4 to CO_2 and H_2O ratio), and significantly diminished growth at greater reducing potential. The jump splines exhibit an inverse relationship between growth temperature and the amount of reductant in the growth atmosphere, that is, less reducing atmospheres require a higher temperature to produce CNTs. This behavior is consistent with a process of thermodynamic origin, since these quantities both contribute to the overall thermodynamic energy.

Computing the Gibbs energy for each experiment requires an approximate overall chemical equation for our CNT synthesis. The overall reaction can be built up from generalized process steps: ethylene reduces iron oxide and forms active metallic iron catalyst, CNTs, and water; and carbon dioxide oxidizes metallic iron. Problematically, there are three primary forms of iron oxide: FeO, Fe_2O_3, and Fe_3O_4. While all of these oxides likely exist on the surface, the final step in the reduction pathway before CNT growth is FeO [49], and additionally, only FeO and Fe_3O_4 can coexist with metallic iron, and FeO is thermodynamically preferred above about 600 K [50,51], so we only consider FeO. This results in the following overall reaction:

$$C_2H_4 + 4FeO \rightleftharpoons CO_2 + C_{CNT} + 4Fe + 2H_2O \tag{1}$$

As a plotting convenience, we will break from chemistry convention and reverse this reaction, placing our desired product on the left. This is done so that Figs. 1 and 2(a) have their regions of reducing conditions in the top right and oxidizing conditions in the bottom left. Reversing the written reaction also has the effect of flipping the sign of all Gibbs energy quantities; spontaneous reactions now have positive Gibbs energy values. This chemical equation then becomes:

$$CO_2 + C_{CNT} + 4Fe + 2H_2O \rightleftharpoons C_2H_4 + 4FeO \tag{2}$$

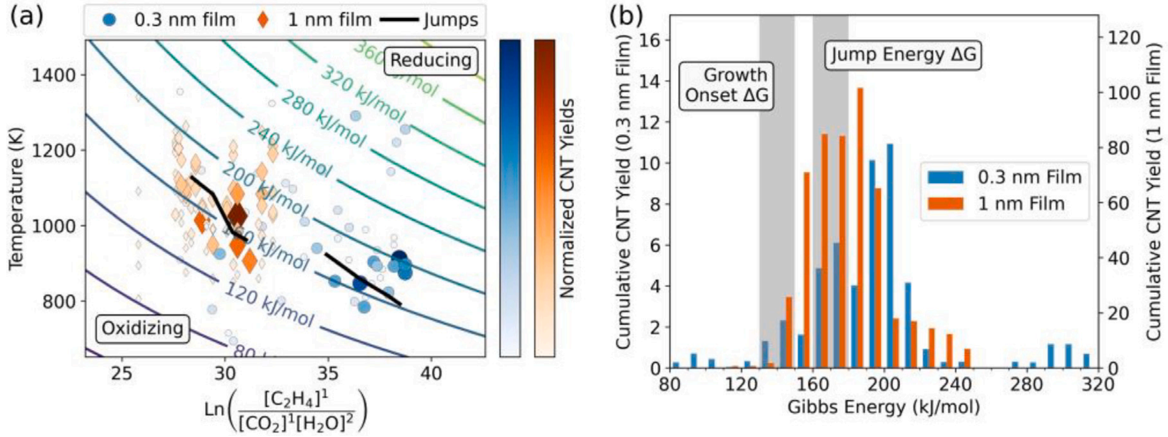

Fig. 2. (a) CNT yield results (same coloring as Fig. 1, size also related to yield) on temperature versus natural log of the reaction quotient Q (Eq. (4)). Contours represent the Gibbs energy at each point. The jump regression discontinuities (black splines) agree with the direction of the Gibbs energy contours, suggesting a thermodynamic origin. The positive Gibbs energy values calculated are consistent with driving the reaction in Eq. (2) to the left (CNT production). The jump regions of best growth for each catalyst thickness separate entirely in thermodynamic space, accompanied by precipitous decline in CNT yield away from the jump region. (b) Cumulative yield via G band area for both campaigns binned by Gibbs energy. Results show the thermodynamic analysis collapses the effects of temperature and the three growth gases into a single Gibbs energy value.

Here we use reversible reaction notation to demonstrate our ability to alter the direction of the reaction by changing the temperature and relative concentrations of the constituent materials. Since C_2H_4 is not thermodynamically stable under the conditions of the reaction, the rightward reaction oxidizing the iron branches, creating trace amounts of carbon, oxygen, and hydrogen containing molecules that we do not believe meaningfully contribute to the reaction due to their low concentrations, combined with the constant gas flow and low reactor residence time ($\ll 1\,\mathrm{s}$ at typical gas flow rates). The change in Gibbs energy for this reaction is

$$\Delta G = \Delta G_0 + RT\ln(Q) \tag{3}$$

with a standard Gibbs energy change of $\Delta G_0 = -90.3\,\mathrm{kJ/mol}$ for reaction (2) [52,53], and where Q is the reaction quotient:

$$Q = \frac{[C_2H_4]^1}{[CO_2]^1[H_2O]^2} \tag{4}$$

Fig. 2(a) shows the experimental results plotted on T vs. $\ln(Q)$ axes, where Q is the reaction quotient shown in Eq. (4), with bulk thermodynamic contours of the Gibbs energy (Eq. (3)) and total CNT yields observed in each campaign as a function of Gibbs energy. Only gasses introduced to the growth chamber were considered in approximating the reaction quotient Q, as well as latent water vapor in the chamber and any water introduced as contamination in the compressed gasses. While water is evolved as a result of the chemistry described in Eq. (2), it is in quantities below the sensitivity of the hygrometer. Fig. 2(b) also shows the cumulative CNT yield binned by Gibbs energy for each film thickness campaign.

Shown on common axes, it is clear that the optimal growth regions identified by the jump splines for each catalyst thickness do not overlap, that is, they share no common reactor conditions that produce significant CNT growth. This demonstrates the extent to which the thickness of the catalyst bed affects the optimal reactor conditions for CNT synthesis. This effect was previously shown by repeating the same reaction over a gradient of catalyst thicknesses, demonstrating an optimal catalyst thickness for a given set of reactor conditions [36], and we show as a complementary result here that optimal and distinct reactor conditions exist for a given catalyst thickness.

The jumps identified by the jump regression planner align well with the thermodynamic contours of Gibbs energy, further indicating they are thermodynamic in origin. We observe that CNT growth occurs only under conditions that favor the reduction of the catalyst metal, that is, at Gibbs energies that drive the reaction leftward. However, growth does not begin at the point at which catalyst reduction is predicted to become spontaneous ($\Delta G = 0$). Fig. 2 shows that both catalyst film thicknesses begin to grow CNTs at conditions where the overall Gibbs energy is $\sim 140\,\mathrm{kJ/mol}$, which we term the growth onset ΔG. Maximum growth is observed at a higher Gibbs energy of $\sim 170\,\mathrm{kJ/mol}$, near the jump identified by the planner. This shows that the reduction of the catalyst material is a necessary, but not sufficient criteria for CNT growth to occur, and this formalism suggests the existence of an additional energetic barrier for effective CNT growth.

This additional energetic barrier could be the result of the catalyst and support forming a mixed metal oxide which is harder to reduce than pure FeO. The alumina catalyst support has been shown to interact strongly with the iron catalyst [33,54,55], and the rough surface and oxygen-deficient nature of ALD alumina promote mixed oxide formation. This mixed oxide should reduce at energies between the reduction of FeO and that of Al_2O_3 [56], which is $\sim 1400\,\mathrm{kJ\,mol^{-1}}$ more difficult to reduce than FeO. The additional $\sim 140\,\mathrm{kJ\,mol^{-1}}$ needed for CNT growth here indicates that the catalyst is behaving like a 90%/10% mix of FeO and Al_2O_3.

We also note that the magnitude of the jump Gibbs energy is similar in magnitude to previous estimates for the activation energy of CNT growth which range from $130\,\mathrm{kJ/mol}$ to $150\,\mathrm{kJ/mol}$ for various reactor systems utilizing both supported and floating iron catalysts [46–48]. This value is commonly attributed to the diffusion of carbon into the catalyst particle due to similarity with the activation energy for the diffusion of carbon in the γ-Fe lattice, although some authors have attributed it to reactant absorption or surface reactions [47].

Since the hydrocarbon fuel concentration increases with increasing reduction potential, we might expect CNT yields to increase as reactor conditions become more reducing, however, we observed a marked decline in the measured G band area. This decline is typically attributed to carbon overcoating the catalyst particle [57], and while this is likely a contributing factor, we propose that increased Ostwald ripening rates are also contributing to faster catalyst death above the jump region. Increased reduction potential with respect to the catalyst increases the driving force for Ostwald ripening, and thereby decreases yield by decreasing catalyst number density and decreasing catalyst lifetime [30,58,59]. Fig. 3 shows representative growth rates for Gibbs energies at, above, and below the jump spline for each catalyst film thickness campaign. The growth rates are determined from the area under the G band for each Raman spectrum collected during the experiment, and the resulting data is fit with the following curve [40]:

$$G(t) = v\tau\left(1 - e^{\frac{-t}{\tau}}\right) \tag{5}$$

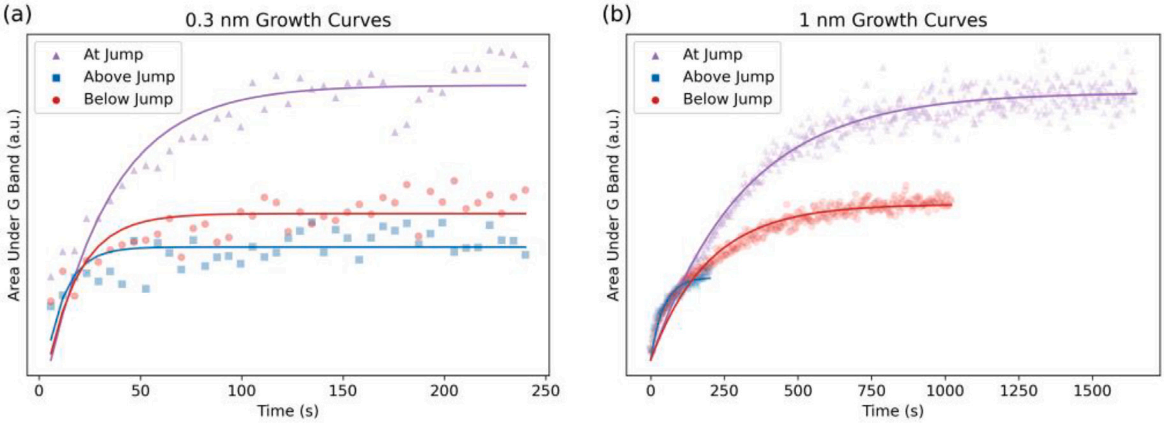

Fig. 3. Sample *in situ* growth curves from 0.3 nm (a) and 1 nm (b) catalyst film thicknesses. Representative dataset is chosen from each region of the results: purple is at the jump region, red is below the jump (more oxidizing), and blue is above the jump region (more reducing). For both catalyst film thicknesses, the experiments all begin at similar growth rates, and decrease at different rates. The most reducing conditions (above jump) see the fastest decline in growth rate and shortest growth duration, followed by conditions more oxidizing than (below) the jump, with the jump region exhibiting both the slowest decline in growth rate and the longest overall growth time. (For interpretation of the references to color in this figure legend, the reader is referred to the web version of this article.)

The fit parameters of the growth curve are the growth rate, v, and the catalyst lifetime, τ. In terms of the lifetime, we see a significant increase at the jump compared to the other conditions. In particular, we see a 20- to 30-fold increase in lifetime in the 0.3 nm Fe film from 1 s to 2 s to 30 s, and a 3- to 5-fold increase in the 1 nm Fe film from ~100 s to ~400 s in the data presented in Fig. 3(b), and up to ~700 s in the most extreme case, not shown since the CNTs began to incandesce towards the end of the growth and saturated the Raman spectrometer. The similar initial slopes of each growth rate curve in Fig. 3 indicate similar levels of catalyst activity at growth onset, when the catalyst material first reduces. In these earliest stages of growth, the nanoparticle catalysts are at their smallest and most numerous and quickly begin to ripen as a function of the reaction conditions [30,33]. The most stable particle diameter under Ostwald ripening is an implicit function of the population diameter distribution, as well as material and environmental terms [58,59]. This leads to the smallest particles experiencing the fastest mass loss and the entire population growing in diameter on average and decreasing in number until the surface-energy driven mass migration is balanced by other material and environmental forces. This earliest Ostwald ripening of the smallest particles is therefore the fastest and most difficult to control, leading to the early decrease in growth rate observed most clearly in Fig. 3(b) as the discrepancy between the fit curves and data points in the earliest seconds of growth, particularly for the results below and at the jump. Above the jump, in more reducing conditions due to higher temperature and carbon and hydrogen concentration, we observe the fastest decline in growth rate and the quickest termination of growth, indicating reducing conditions accelerate catalyst deactivation. Below the jump, where CNT growth occurs, growth rates decline slower, and prolonged growth is observed compared to growth above the jump, indicating that more oxidizing conditions are conducive to increased catalyst lifetimes. These effects reach a balance at the jump region, where the growth rate declines the slowest, and the longest overall growth durations are observed, demonstrating that operating in as oxidizing an environment as possible slows catalyst deactivation.

The best observed catalyst lifetimes are on the order of one to several minutes, which are consistent with previous results from our group [20,21,36–38,40], but short compared to many supported catalyst literature results. We believe there are a few contributing factors to our overall shorter than average lifetimes due to the specifics of the setup, that do not preclude these results from being applicable in a general supported catalyst setting. The two biggest differences between our experimental setup compared to typical supported catalyst systems in the literature are that our reactions are performed at low pressure, 10 Torr in this case, and that we explicitly desire sparse growth, not forests, since the CNT forest occludes the silicon substrate from the laser, which is where we derive our temperature feedback.

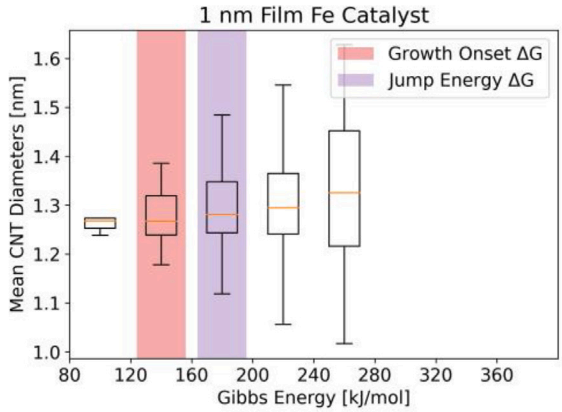

Fig. 4. Average CNT diameter distributions for the 1 nm Fe **(b)** campaign as a function of the Gibbs energy. Raman spectra were collected using 532 nm, 633 nm, and 785 nm lasers. Mean diameters were calculated by finding the intensity-weighted average RBM location [11] for each laser individually, then binning each laser line result in a given Gibbs energy range. The distribution of average diameters narrows as the reaction becomes more oxidizing (lower Gibbs energy), indicating better control of CNT diameters under these conditions, and therefore better control of the Ostwald ripening of the catalyst bed.

Consistent with slowed Ostwald ripening kinetics resulting in a prolonged smaller diameter and more numerous nanoparticle catalyst bed are the observed average diameters of CNTs near the jump. Fig. 4 shows the distribution of average CNT diameters as a function of Gibbs energy. Three Raman laser lines were used to collect the diameter information: 532 nm, 633 nm, and 785 nm. To determine the average CNT diameter in a given Raman spectrum, an intensity-weighted average of the RBM region is calculated between 80 cm^{-1} and 280 cm^{-1} [11], and converted to a diameter using the equation:

$$d_t = \frac{227}{\sqrt{\omega_{RBM}^2 + 0.05786}} \tag{6}$$

where d_t is the CNT diameter, ω_{RBM} is the RBM frequency in cm^{-1}, and the values 227 and 0.057 86 are fit and environmental parameters, respectively, whose values were determined in the same work that produced the equation [60]. An average diameter was determined for each Raman laser line, and individually contribute to the distributions in Fig. 4, which are grouped by reaction Gibbs energy similarly to Fig. 2(b). In some cases, RBMs were observed for some but not all excitation wavelengths. In these cases, that laser was excluded from the distributions in Fig. 4. As the Gibbs energy trends towards more reducing conditions (higher Gibbs energies), the spread of average diameter increases, indicating a greater spread of nanoparticle catalyst diameters. This is consistent with poor control of Ostwald ripening. This trend is clearly observed in the 1 nm catalyst film. In the case of the 0.3 nm film (Figure S2), we observed similar diameter distributions across all Gibbs energy values. We believe this difference is due to the increased relative impact of catalyst subsurface diffusion on the thinner film.

4. Conclusion

By autonomously performing CNT growth experiments across two catalyst thicknesses and a wide range of temperatures and growth atmosphere compositions, we find optimal growth conditions for each catalyst thickness lay along a narrow band in thermodynamic space. The thermodynamic regions of optimal growth, while energetically very similar, do not overlap one another for the two catalyst thicknesses tested here, and indeed, yield declines precipitously outside the narrow respective optima. The optimal growth splines were determined using an active learning jump regression algorithm targeting the largest yield discontinuity within thermodynamic space. The mechanism behind these discontinuities is posited to be either catalyst metal oxide reduction or an activation energy beyond catalyst reduction, likely diffusion of carbon atoms through the iron catalyst particles.

This work identifies narrow thermodynamic islands of optimal CNT growth with no overlap between regions for the two catalyst film thicknesses tested (0.3 nm and 1 nm), demonstrating the powerful effect of catalyst thickness on CNT yields for fixed reactor conditions. It also offers salvation from this effect: demonstrating that different reactor conditions are required to optimize different catalyst thicknesses, and indeed, that different catalyst thicknesses can be optimized at all.

In addition to the yield gains observed near the jump, we observe longest catalyst lifetimes and the best control over CNT diameters. We attribute this behavior to thermodynamic control of nanoparticle catalyst kinetics, inhibiting Ostwald ripening by conducting CNT growth in the most oxidizing conditions that will sustain it. Our thermodynamic treatment of catalyst reduction in CNT growth coupled with the jump regression algorithm provides a generalizable approach for further study of different metal catalysts, as well as a roadmap to create engineering tools to scale CNT production, and highlights the importance and capabilities of autonomous, hypothesis-driven machine learning experimentation in materials science.

CRediT authorship contribution statement

Robert Waelder: Writing – review & editing, Writing – original draft, Visualization, Software, Methodology, Investigation, Formal analysis. **Chiwoo Park:** Software, Methodology, Formal analysis. **Arthur Sloan:** Writing – review & editing, Formal analysis. **Jennifer Carpena-Núñez:** Methodology, Investigation, Formal analysis, Data curation. **Joshua Yoho:** Validation. **Stephane Gorsse:** Writing – review & editing, Validation, Methodology. **Rahul Rao:** Writing – review & editing, Investigation, Formal analysis, Data curation. **Benji Maruyama:** Writing – review & editing, Supervision, Resources, Project administration, Investigation, Conceptualization.

Declaration of competing interest

The authors declare that they have no known competing financial interests or personal relationships that could have appeared to influence the work reported in this paper.

Acknowledgments

We acknowledge funding from the Air Force Office of Scientific Research, LRIR, USA #19RXCOR040. Park's work is partially supported by the National Science Foundation, United States (NSF-2152655). This research was performed while Arthur Sloan held an NRC Research Associateship award at AFRL.

Appendix A. Supplementary data

Supplementary material related to this article can be found online at https://doi.org/10.1016/j.carbon.2024.119356.

References

[1] M.F.L. De Volder, S.H. Tawfick, R.H. Baughman, A.J. Hart, Carbon nanotubes: Present and future commercial applications, Science 339 (6119) (2013) 535–539, http://dx.doi.org/10.1126/science.1222453, URL https://www.science.org/doi/10.1126/science.1222453.

[2] H. Xu, S.M. Anlage, L. Hu, G. Gruner, Microwave shielding of transparent and conducting single-walled carbon nanotube films, Appl. Phys. Lett. 90 (18) (2007) 183119, http://dx.doi.org/10.1063/1.2734897, URL http://aip.scitation.org/doi/10.1063/1.2734897.

[3] X. He, W. Gao, L. Xie, B. Li, Q. Zhang, S. Lei, J.M. Robinson, E.H. Hároz, S.K. Doorn, W. Wang, R. Vajtai, P.M. Ajayan, W.W. Adams, R.H. Hauge, J. Kono, Wafer-scale monodomain films of spontaneously aligned single-walled carbon nanotubes, Nature Nanotechnol. 11 (7) (2016) 633–638, http://dx.doi.org/10.1038/nnano.2016.44, URL http://www.nature.com/articles/nnano.2016.44.

[4] S. Park, M. Vosguerichian, Z. Bao, A review of fabrication and applications of carbon nanotube film-based flexible electronics, Nanoscale 5 (5) (2013) 1727, http://dx.doi.org/10.1039/c3nr33560g, URL http://xlink.rsc.org/?DOI=c3nr33560g.

[5] A. Mikhalchan, J.J. Vilatela, A perspective on high-performance CNT fibres for structural composites, Carbon 150 (2019) 191–215, http://dx.doi.org/10.1016/j.carbon.2019.04.113, URL https://linkinghub.elsevier.com/retrieve/pii/S0008622319304567.

[6] C. Jiang, A. Saha, C.C. Young, D.P. Hashim, C.E. Ramirez, P.M. Ajayan, M. Pasquali, A.A. Martí, Macroscopic nanotube fibers spun from single-walled carbon nanotube polyelectrolytes, ACS Nano 8 (9) (2014) 9107–9112, http://dx.doi.org/10.1021/nn502552q, URL https://pubs.acs.org/doi/10.1021/nn502552q.

[7] M. Zhang, S. Fang, A.A. Zakhidov, S.B. Lee, A.E. Aliev, C.D. Williams, K.R. Atkinson, R.H. Baughman, Strong, transparent, multifunctional, carbon nanotube sheets, Science 309 (5738) (2005) 1215–1219, http://dx.doi.org/10.1126/science.1115311, URL https://www.science.org/doi/10.1126/science.1115311.

[8] B. Vigolo, A. Pénicaud, C. Coulon, C. Sauder, R. Pailler, C. Journet, P. Bernier, P. Poulin, Dispersions and fibers of carbon nanotubes, MRS Proc. 633 (2000) A12.1, http://dx.doi.org/10.1557/PROC-633-A12.1, URL http://link.springer.com/10.1557/PROC-633-A12.1.

[9] N. Bajwa, X. Li, P.M. Ajayan, R. Vajtai, Mechanisms for catalytic CVD growth of multiwalled carbon nanotubes, J. Nanosci. Nanotechnol. 8 (11) (2008) 6054–6064, http://dx.doi.org/10.1166/jnn.2008.SW02, URL https://www.ingentaconnect.com/content/10.1166/jnn.2008.SW02.

[10] A.O.M. Alzahrani, M. Alayash, S. Alghamdi, A simple method to form a forest of carbon nanotube bundles during growth stage, SN Appl. Sci. 4 (8) (2022) 218, http://dx.doi.org/10.1007/s42452-022-05083-z, URL https://link.springer.com/10.1007/s42452-022-05083-z.

[11] J.S. Bulmer, A.W. Sloan, M. Glerum, J. Carpena-Núñez, R. Waelder, J. Humes, A.M. Boies, M. Pasquali, R. Rao, B. Maruyama, Forecasting carbon nanotube diameter in floating catalyst chemical vapor deposition, Carbon 201 (2023) 719–733, http://dx.doi.org/10.1016/j.carbon.2022.08.001, URL https://linkinghub.elsevier.com/retrieve/pii/S0008622322006145.

[12] X.-Q. Li, S. Jiang, L. Zhang, M.-K. Zou, Y. Jian, D.-M. Sun, P.-X. Hou, H.-M. Cheng, C. Liu, Preparation of isolated semiconducting single-wall carbon nanotubes by oxygen-assisted floating catalyst chemical vapor deposition, Chem. Eng. J. 450 (2022) 137861, http://dx.doi.org/10.1016/j.cej.2022.137861, URL https://linkinghub.elsevier.com/retrieve/pii/S1385894722033484.

[13] S. Hao, L. Qian, Q. Wu, D. Li, F. Han, L. Feng, L. Xin, T. Yang, S. Wang, J. Zhang, M. He, Subnanometer single-walled carbon nanotube growth from Fe-containing layered double hydroxides, Chem. Eng. J. 446 (2022) 137087, http://dx.doi.org/10.1016/j.cej.2022.137087, URL https://linkinghub.elsevier.com/retrieve/pii/S1385894722025797.

[14] A. Maiti, C.J. Brabec, C. Roland, J. Bernholc, Theory of carbon nanotube growth, Phys. Rev. B 52 (20) (1995) 14850–14858, http://dx.doi.org/10.1103/PhysRevB.52.14850, URL https://link.aps.org/doi/10.1103/PhysRevB.52.14850.

[15] K. Bolton, F. Ding, A. Rosén, Atomistic simulations of catalyzed carbon nanotube growth, J. Nanosci. Nanotechnol. 6 (5) (2006) 1211–1224, http://dx.doi.org/10.1166/jnn.2006.145, URL http://www.ingentaselect.com/rpsv/cgi-bin/cgi?ini=xref&body=linker&reqdoi=10.1166/jnn.2006.145.

[16] H. Duan, A. Rosén, A. Harutyunyan, S. Curtarolo, K. Bolton, Computational studies of small carbon and iron-carbon systems relevant to carbon nanotube growth, J. Nanosci. Nanotechnol. 8 (11) (2008) 6170–6177, http://dx.doi.org/10.1166/jnn.2008.SW12, URL https://www.ingentaconnect.com/content/10.1166/jnn.2008.SW12.

[17] T. Oke, S. Hontinfinde, M. Karimou, F. Zounmenou, F. Hontinfinde, Atomistic growth model with edge diffusion for chiral carbon nanotubes, Phys. E: Low-dimens. Syst. Nanostruct. 142 (2022) 115298, http://dx.doi.org/10.1016/j.physe.2022.115298, URL https://linkinghub.elsevier.com/retrieve/pii/S1386947722001461.

[18] F. Zounmenou, R. Hontinfinde, F. Hontinfinde, Growth kinetics of a single-walled carbon nanotube: Exact and simulation results, Phys. A 594 (2022) 127013, http://dx.doi.org/10.1016/j.physa.2022.127013, URL https://linkinghub.elsevier.com/retrieve/pii/S0378437122000899.

[19] G.D. Förster, T.D. Swinburne, H. Jiang, E. Kauppinen, C. Bichara, A semi-grand canonical kinetic Monte Carlo study of single-walled carbon nanotube growth, AIP Adv. 11 (4) (2021) 045306, http://dx.doi.org/10.1063/5.0030943, URL https://aip.scitation.org/doi/10.1063/5.0030943.

[20] R. Rao, C.L. Pint, A.E. Islam, R.S. Weatherup, S. Hofmann, E.R. Meshot, F. Wu, C. Zhou, N. Dee, P.B. Amama, J. Carpena-Nuñez, W. Shi, D.L. Plata, E.S. Penev, B.I. Yakobson, P.B. Balbuena, C. Bichara, D.N. Futaba, S. Noda, H. Shin, K.S. Kim, B. Simard, F. Mirri, M. Pasquali, F. Fornasiero, E.I. Kauppinen, M. Arnold, B.A. Cola, P. Nikolaev, S. Arepalli, H.-M. Cheng, D.N. Zakharov, E.A. Stach, J. Zhang, F. Wei, M. Terrones, D.B. Geohegan, B. Maruyama, S. Maruyama, Y. Li, W.W. Adams, A.J. Hart, Carbon nanotubes and related nanomaterials: Critical advances and challenges for synthesis toward mainstream commercial applications, ACS Nano 12 (12) (2018) 11756–11784, http://dx.doi.org/10.1021/acsnano.8b06511, URL https://pubs.acs.org/doi/10.1021/acsnano.8b06511.

[21] R. Rao, N. Pierce, D. Liptak, D. Hooper, G. Sargent, S.L. Semiatin, S. Curtarolo, A.R. Harutyunyan, B. Maruyama, Revealing the impact of catalyst phase transition on carbon nanotube growth by *in Situ* Raman spectroscopy, ACS Nano 7 (2) (2013) 1100–1107, http://dx.doi.org/10.1021/nn304064u, URL https://pubs.acs.org/doi/10.1021/nn304064u.

[22] A.G. Nasibulin, P.V. Pikhitsa, H. Jiang, E.I. Kauppinen, Correlation between catalyst particle and single-walled carbon nanotube diameters, Carbon 43 (11) (2005) 2251–2257, http://dx.doi.org/10.1016/j.carbon.2005.03.048, URL https://linkinghub.elsevier.com/retrieve/pii/S0008622305002101.

[23] M.-F.C. Fiawoo, A.-M. Bonnot, H. Amara, C. Bichara, J. Thibault-Pénisson, A. Loiseau, Evidence of correlation between catalyst particles and the single-wall carbon nanotube diameter: A first step towards chirality control, Phys. Rev. Lett. 108 (19) (2012) 195503, http://dx.doi.org/10.1103/PhysRevLett.108.195503, URL https://link.aps.org/doi/10.1103/PhysRevLett.108.195503.

[24] F. Yang, H. Zhao, R. Li, Q. Liu, X. Zhang, X. Bai, R. Wang, Y. Li, Growth modes of single-walled carbon nanotubes on catalysts, Sci. Adv. 8 (41) (2022) eabq0794, http://dx.doi.org/10.1126/sciadv.abq0794, URL https://www.science.org/doi/10.1126/sciadv.abq0794.

[25] J.S. Bulmer, A. Kaniyoor, J.A. Elliott, A meta-analysis of conductive and strong carbon nanotube materials, Adv. Mater. 33 (36) (2021) 2008432, http://dx.doi.org/10.1002/adma.202008432, URL https://onlinelibrary.wiley.com/doi/10.1002/adma.202008432.

[26] Q. Zhang, E.H. Hároz, Z. Jin, L. Ren, X. Wang, R.S. Arvidson, A. Lüttge, J. Kono, Plasmonic nature of the terahertz conductivity peak in single-wall carbon nanotubes, Nano Lett. 13 (12) (2013) 5991–5996, http://dx.doi.org/10.1021/nl403175g, URL https://pubs.acs.org/doi/10.1021/nl403175g.

[27] R.H. Tunuguntla, R.Y. Henley, Y.-C. Yao, T.A. Pham, M. Wanunu, A. Noy, Enhanced water permeability and tunable ion selectivity in subnanometer carbon nanotube porins, Science 357 (6353) (2017) 792–796, http://dx.doi.org/10.1126/science.aan2438, URL https://www.science.org/doi/10.1126/science.aan2438.

[28] H.Y. Jung, S.M. Jung, L. Kim, J.S. Suh, A simple method to control the diameter of carbon nanotubes and the effect of the diameter in field emission, Carbon 46 (6) (2008) 969–973, http://dx.doi.org/10.1016/j.carbon.2008.03.006, URL https://linkinghub.elsevier.com/retrieve/pii/S0008622308001395.

[29] A. Moisala, A.G. Nasibulin, E.I. Kauppinen, The role of metal nanoparticles in the catalytic production of single-walled carbon nanotubes—A review, J. Phys.: Condens. Matter. 15 (42) (2003) S3011–S3035, http://dx.doi.org/10.1088/0953-8984/15/42/003, URL https://iopscience.iop.org/article/10.1088/0953-8984/15/42/003.

[30] P.B. Amama, C.L. Pint, L. McJilton, S.M. Kim, E.A. Stach, P.T. Murray, R.H. Hauge, B. Maruyama, Role of water in super growth of single-walled carbon nanotube carpets, Nano Lett. 9 (1) (2009) 44–49, http://dx.doi.org/10.1021/nl801876h, URL https://pubs.acs.org/doi/10.1021/nl801876h.

[31] S. Jeong, J. Lee, H.-C. Kim, J.Y. Hwang, B.-C. Ku, D.N. Zakharov, B. Maruyama, E.A. Stach, S.M. Kim, Direct observation of morphological evolution of a catalyst during carbon nanotube forest growth: New insights into growth and growth termination, Nanoscale 8 (4) (2016) 2055–2062, http://dx.doi.org/10.1039/C5NR05547D, URL http://xlink.rsc.org/?DOI=C5NR05547D.

[32] S.M. Kim, C.L. Pint, P.B. Amama, D.N. Zakharov, R.H. Hauge, B. Maruyama, E.A. Stach, Evolution in catalyst morphology leads to carbon nanotube growth termination, J. Phys. Chem. Lett. 1 (6) (2010) 918–922, http://dx.doi.org/10.1021/jz9004762, URL https://pubs.acs.org/doi/10.1021/jz9004762.

[33] P.B. Amama, C.L. Pint, S.M. Kim, L. McJilton, K.G. Eyink, E.A. Stach, R.H. Hauge, B. Maruyama, Influence of alumina type on the evolution and activity of alumina-supported fe catalysts in single-walled carbon nanotube carpet growth, ACS Nano 4 (2) (2010) 895–904, http://dx.doi.org/10.1021/nn901700u, URL https://pubs.acs.org/doi/10.1021/nn901700u.

[34] A. La Cava, C. Bernardo, D. Trimm, Studies of deactivation of metals by carbon deposition, Carbon 20 (3) (1982) 219–223, http://dx.doi.org/10.1016/0008-6223(82)90024-0, URL https://linkinghub.elsevier.com/retrieve/pii/0008622382900240.

[35] M. Stadermann, S.P. Sherlock, J.-B. In, F. Fornasiero, H.G. Park, A.B. Artyukhin, Y. Wang, J.J. De Yoreo, C.P. Grigoropoulos, O. Bakajin, A.A. Chernov, A. Noy, Mechanism and kinetics of growth termination in controlled chemical vapor deposition growth of multiwall carbon nanotube arrays, Nano Lett. 9 (2) (2009) 738–744, http://dx.doi.org/10.1021/nl803277g, URL https://pubs.acs.org/doi/10.1021/nl803277g.

[36] R. Rao, J. Carpena-Núñez, N.T. Dee, D.N. Zakharov, J.A. Boscoboinik, E.A. Stach, A.J. Hart, B. Maruyama, Maximization of carbon nanotube yield by solid carbon-assisted dewetting of iron catalyst films, Carbon 165 (2020) 251–258, http://dx.doi.org/10.1016/j.carbon.2020.04.064, URL https://linkinghub.elsevier.com/retrieve/pii/S0008622320303936.

[37] P. Nikolaev, D. Hooper, N. Perea-López, M. Terrones, B. Maruyama, Discovery of wall-selective carbon nanotube growth conditions *via* automated experimentation, ACS Nano 8 (10) (2014) 10214–10222, http://dx.doi.org/10.1021/nn503347a, URL https://pubs.acs.org/doi/10.1021/nn503347a.

[38] P. Nikolaev, D. Hooper, F. Webber, R. Rao, K. Decker, M. Krein, J. Poleski, R. Barto, B. Maruyama, Autonomy in materials research: A case study in carbon nanotube growth, npj Comput. Mater. 2 (1) (2016) 16031, http://dx.doi.org/10.1038/npjcompumats.2016.31, URL http://www.nature.com/articles/npjcompumats201631.

[39] E. Stach, B. DeCost, A.G. Kusne, J. Hattrick-Simpers, K.A. Brown, K.G. Reyes, J. Schrier, S. Billinge, T. Buonassisi, I. Foster, C.P. Gomes, J.M. Gregoire, A. Mehta, J. Montoya, E. Olivetti, C. Park, E. Rotenberg, S.K. Saikin, S. Smullin, V. Stanev, B. Maruyama, Autonomous experimentation systems for materials development: A community perspective, Matter 4 (9) (2021) 2702–2726, http://dx.doi.org/10.1016/j.matt.2021.06.036, URL https://linkinghub.elsevier.com/retrieve/pii/S2590238521003064.

[40] R. Rao, D. Liptak, T. Cherukuri, B.I. Yakobson, B. Maruyama, In situ evidence for chirality-dependent growth rates of individual carbon nanotubes, Nature Mater. 11 (3) (2012) 213–216, http://dx.doi.org/10.1038/nmat3231, URL https://www.nature.com/articles/nmat3231.

[41] R. Rao, J. Carpena-Núñez, P. Nikolaev, M.A. Susner, K.G. Reyes, B. Maruyama, Advanced machine learning decision policies for diameter control of carbon nanotubes, npj Comput. Mater. 7 (1) (2021) 157, http://dx.doi.org/10.1038/s41524-021-00629-y, URL https://www.nature.com/articles/s41524-021-00629-y.

[42] J. Chang, P. Nikolaev, J. Carpena-Núñez, R. Rao, K. Decker, A.E. Islam, J. Kim, M.A. Pitt, J.I. Myung, B. Maruyama, Efficient closed-loop maximization of carbon nanotube growth rate using Bayesian optimization, Sci. Rep. 10 (1) (2020) 9040, http://dx.doi.org/10.1038/s41598-020-64397-3, URL http://www.nature.com/articles/s41598-020-64397-3.

[43] C. Park, Jump Gaussian process model for estimating piecewise continuous regression functions, J. Mach. Learn. Res. 23 (278) (2022) 1–37, URL http://jmlr.org/papers/v23/21-1472.html.

[44] C. Park, R. Waelder, B. Kang, B. Maruyama, S. Hong, R. Gramacy, Active learning of piecewise Gaussian process surrogates, 2023, http://dx.doi.org/10.48550/arXiv.2301.08789, arXiv:2301.08789 [cs, stat]. URL http://arxiv.org/abs/2301.08789.

[45] M.D. Mckay, R.J. Beckman, W.J. Conover, A comparison of three methods for selecting values of input variables in the analysis of output from a computer code, Technometrics 42 (1) (2000) 55–61, http://dx.doi.org/10.1080/00401706.2000.10485979, URL http://www.tandfonline.com/doi/abs/10.1080/00401706.2000.10485979.

[46] Y.T. Lee, N.S. Kim, J. Park, J.B. Han, Y.S. Choi, H. Ryu, H.J. Lee, Temperature-dependent growth of carbon nanotubes by pyrolysis of ferrocene and acetylene in the range between 700 and 1000 °C, Chem. Phys. Lett. 372 (5–6) (2003) 853–859, http://dx.doi.org/10.1016/S0009-2614(03)00529-3, URL https://linkinghub.elsevier.com/retrieve/pii/S0009261403005293.

[47] S.L. Pirard, S. Douven, C. Bossuot, G. Heyen, J.-P. Pirard, A kinetic study of multi-walled carbon nanotube synthesis by catalytic chemical vapor deposition using a Fe–Co/Al2O3 catalyst, Carbon 45 (6) (2007) 1167–1175, http://dx.doi.org/10.1016/j.carbon.2007.02.021, URL https://linkinghub.elsevier.com/retrieve/pii/S0008622307000826.

[48] A.S. Anisimov, A.G. Nasibulin, H. Jiang, P. Launois, J. Cambedouzou, S.D. Shandakov, E.I. Kauppinen, Mechanistic investigations of single-walled carbon nanotube synthesis by ferrocene vapor decomposition in carbon monoxide, Carbon 48 (2) (2010) 380–388, http://dx.doi.org/10.1016/j.carbon.2009.09.040, URL https://linkinghub.elsevier.com/retrieve/pii/S0008622309006071.

[49] J. Carpena-Núñez, J.A. Boscoboinik, S. Saber, R. Rao, J.-Q. Zhong, M.R. Maschmann, P.R. Kidambi, N.T. Dee, D.N. Zakharov, A.J. Hart, E.A. Stach, B. Maruyama, Isolating the roles of hydrogen exposure and trace carbon contamination on the formation of active catalyst populations for carbon nanotube growth, ACS Nano 13 (8) (2019) 8736–8748, http://dx.doi.org/10.1021/acsnano.9b01382, URL https://pubs.acs.org/doi/10.1021/acsnano.9b01382.

[50] D. Spreitzer, J. Schenk, Reduction of iron oxides with hydrogen—A review, Steel Res. Int. 90 (10) (2019) 1900108, http://dx.doi.org/10.1002/srin.201900108, URL https://onlinelibrary.wiley.com/doi/10.1002/srin.201900108.

[51] M. Kinaci, T. Lichtenegger, S. Schneiderbauer, A CFD-DEM model for the simulation of direct reduction of iron-ore in fluidized beds, Chem. Eng. Sci. 227 (2020) 115858, http://dx.doi.org/10.1016/j.ces.2020.115858, URL https://linkinghub.elsevier.com/retrieve/pii/S0009250920303900.

[52] T.C. Allison, NIST-JANAF thermochemical tables - SRD 13, 2013, http://dx.doi.org/10.18434/T42S31, URL https://janaf.nist.gov/.

[53] J. Mentado-Morales, G. Mendoza-Pérez, Á.E. De Los Santos-Acosta, E. Peralta-Reyes, A. Regalado-Méndez, Energies of combustion and enthalpies of formation of carbon nanotubes, J. Therm. Anal. Calorim. 131 (3) (2018) 2763–2768, http://dx.doi.org/10.1007/s10973-017-6741-2.

[54] S. Noda, K. Hasegawa, H. Sugime, K. Kakehi, Z. Zhang, S. Maruyama, Y. Yamaguchi, Millimeter-thick single-walled carbon nanotube forests: Hidden role of catalyst support, Japan. J. Appl. Phys. 46 (5L) (2007) L399, http://dx.doi.org/10.1143/JJAP.46.L399, URL https://iopscience.iop.org/article/10.1143/JJAP.46.L399.

[55] S. Miura, Y. Yoshihara, M. Asaka, K. Hasegawa, H. Sugime, A. Ota, H. Oshima, S. Noda, Millimeter-tall carbon nanotube arrays grown on aluminum substrates, Carbon 130 (2018) 834–842, http://dx.doi.org/10.1016/j.carbon.2018.01.075, URL https://linkinghub.elsevier.com/retrieve/pii/S0008622318300848.

[56] B. Pint, J. Schneibel, The effect of carbon and reactive element dopants on oxidation lifetime of FeAl, Scr. Mater. 52 (12) (2005) 1199–1204, http://dx.doi.org/10.1016/j.scriptamat.2005.03.008, URL https://linkinghub.elsevier.com/retrieve/pii/S1359646205001466.

[57] L. Zhang, M. He, T.W. Hansen, J. Kling, H. Jiang, E.I. Kauppinen, A. Loiseau, J.B. Wagner, Growth termination and multiple nucleation of single-wall carbon nanotubes evidenced by *in Situ* transmission electron microscopy, ACS Nano 11 (5) (2017) 4483–4493, http://dx.doi.org/10.1021/acsnano.6b05941, URL https://pubs.acs.org/doi/10.1021/acsnano.6b05941.

[58] P.W. Voorhees, The theory of Ostwald ripening, J. Stat. Phys. 38 (1–2) (1985) 231–252, http://dx.doi.org/10.1007/BF01017860, URL http://link.springer.com/10.1007/BF01017860.

[59] R. Ouyang, J.-X. Liu, W.-X. Li, Atomistic theory of ostwald ripening and disintegration of supported metal particles under reaction conditions, J. Am. Chem. Soc. 135 (5) (2013) 1760–1771, http://dx.doi.org/10.1021/ja3087054, URL https://pubs.acs.org/doi/10.1021/ja3087054.

[60] P.T. Araujo, I.O. Maciel, P.B.C. Pesce, M.A. Pimenta, S.K. Doorn, H. Qian, A. Hartschuh, M. Steiner, L. Grigorian, K. Hata, A. Jorio, Nature of the constant factor in the relation between radial breathing mode frequency and tube diameter for single-wall carbon nanotubes, Phys. Rev. B 77 (24) (2008) 241403, http://dx.doi.org/10.1103/PhysRevB.77.241403, URL https://link.aps.org/doi/10.1103/PhysRevB.77.241403.